ARTICLE

Check for updates

Possible warming effect of fine particulate matter in the atmosphere

Shau-Liang Chen[1], Sih-Wei Chang[1], Yen-Jen Chen[1] & Hsuen-Li Chen [1,2]✉

Particulate matter emitted through human activities not only pollutes the air, but also cools the Earth by scattering shortwave solar radiation. However, coarser dust particles have been found to exert a warming effect that could, to some extent compensate for the cooling effect of fine dust. Here we investigate the radiative effects of sulfate containing aerosols of various sizes and core/shell structures using Mie scattering and three-dimensional finite difference time domain simulations of the electromagnetic fields inside and around particulate matter particles. We find that not only coarse dust, but also fine non-light-absorbing inorganic aerosols such as sulfate can have a warming effect. Specifically, although the opacity of fine particles decreases at longer wavelengths, they can strongly absorb and re-emit thermal radiation under resonance conditions at long wavelength. We suggest that these effects need to be taken into account when assessing the contribution of aerosols to climate change.

[1] Department of Materials Science and Engineering, National Taiwan University, No. 1, Sec. 4, Roosevelt Road, Taipei 10617, Taiwan. [2] Center of Atomic Initiative for New Materials, National Taiwan University, Taipei 10617, Taiwan. ✉email: hsuenlichen@ntu.edu.tw

During the last decade, global warming has led to climate change and has triggered more extreme weather events, hotter heat waves[1], drier droughts[2], colder winters[3], and larger storm surges[4], endangering the survival of flora and fauna on Earth, including human beings. To achieve the Paris Agreement aims, it will be necessary to strictly limit the total amount of cumulative carbon emissions[5–8]. On the other hand, particulate matter (PM) generated by human activities not only pollute the air, but also affect Earth's radiation budget[9]. The radiative effect of PM is the opposite of that of greenhouse gases. The direct scattering of short wavelength solar radiation by anthropogenic PM particles increase planetary albedo, thereby exerting a cooling influence on the planet[10,11]. The global mean radiative forcing due to aerosol–radiation interactions is $\sim-0.35\,\mathrm{W\,m^{-2}}$; aerosol–cloud interactions is $\sim-0.45\,\mathrm{W\,m^{-2}}$; greenhouse gases is $\sim+2.83\,\mathrm{W\,m^{-2}}$ [12].

Anthropogenic PM includes secondary organic aerosols and secondary inorganic aerosols (SIA), the main components of SIA are sulfate and nitrate[13–15]. SIA particles are taken as the portion of Aitken and Accumulation mode particles[16,17]. In previous studies, it was concluded that sulfate also absorb longwave radiation, but the aerosol radiative effect is generally small because the opacity of aerosols decreases in longer wavelengths of infrared (IR) regime[11]. The major natural sources of ambient PM, such as marine aerosol, mineral dust, Saharan dust, smoke plumes, and their mixtures have been found to enhance the greenhouse effect[18–24]. Recently literature found that the dust in the atmosphere is substantially coarser than represented in current global climate models. They also found the contribution of very coarse dust (diameter ≥5 μm) was underestimated, and the coarse particles could cause warming of the atmosphere[24]. More recently, they stated that climate models consistently underestimate the amount of coarse dust in the atmosphere, and the climate model must be revised[25]. The improved description of the dust size distribution and its vertical distribution, as well as the IR optical properties, are important for a reliable estimate of its radiation effects[23].

The atmosphere often contains a mixture of different types of PM particles, and the mixing process leads to change in sulfate and mineral dust loads, thus altering their impact on the atmospheric radiation. Transmission electron microscopy (TEM) has been used to observe the size, structure and composition of individual fine particles, which is essential for assessing the radiation properties of PM particles and understanding their climatic effects[26,27]. It has been observed that mineral dust particles often get coated with sulfates and other soluble materials[28]. The fine ($PM_{2.5}$) and coarse (PM_{10}) particles were intended to apply to the two major atmospheric particle distributions which overlap in the intermodal size range between 1 and 3 μm[17,29]. The interaction of the composite PM particles with atmospheric radiation may be different from that of homogeneous PM particles. Theoretical analysis of the relationship between various types of PM mixtures, particles sizes, absorption coefficients, and wavelength are important for the investigation on radiative properties and climate modeling. The atmospheric window offers a direct and strong driving force to dissipate heat into space in the form of thermal radiation under appropriate atmospheric conditions[30–34]. The application of radiative cooling as a passive cooling option for buildings has a great potential to compensate the problems raised by global warming[35,36]. The PM in the atmospheric window would affect the absorption and scattering effects of thermal radiation[37].

In this paper, we discuss the thermal radiation properties of sulfate and SiO_2/sulfate core/shell mixture particles in atmospheric window, including ED and MD resonance behavior. We also used the three-dimensional finite difference time domain (3D-FDTD) method to simulate the electromagnetic fields inside and around PM particles with various sizes and core/shell structures. In this study, we used the World Health Organization air quality guidelines values to simplify the calculation of thermal radiation power density changes in a clear atmosphere with and without PM particles. These calculations of power density changes preclude any differences in geographical and seasonal distributions. From the conceptual experimental results, it was found that different optical properties related to particle size have a significant effect on the thermal emissivity, potentially affecting the temperature of the surrounding environment.

Results and discussion

The atmosphere has a highly transparent window for IR wavelengths in the range from 8 to 13 μm [the so-called first infrared atmospheric window (IRW1)] and a relatively transparent window for IR wavelengths in the range from 16 to 24 μm [the so-called second infrared atmospheric window (IRW2)]; they are highlighted by the light-cyan and yellow areas, respectively, in Fig. 1a. According to Planck's law and Wien's displacement law, when the surface temperature is 250, 300, and 350 K, the corresponding maximum wavelengths λ_{max} of the thermal radiation are 11.51, 9.50, and 8.25 μm, respectively. These thermal radiation peaks from the Earth's surface coincidentally fall within the IRW1. For these same temperatures, ~31, 38, and 41%, respectively, of the thermal radiation energy distribution is concentrated in IRW1, and ~29, 24, and 20%, respectively, in IRW2. The higher the surface temperature, the greater the effect of IRW1 on thermal radiation; furthermore, the effect of IRW1 will also be greater than that of IRW2. This feature of IRW1 permits heat to dissipate through thermal radiation emission, with the potential to provide a passive cooling mechanism for the Earth.

A recent report displays that the main constituents of both PM_{10} and $PM_{2.5}$ particles are generally organic matter, sulfate, and nitrate[38]. Figure 1b–e present the IR absorbance spectra of the major components of SIA—$(NH_4)_2SO_4$, NH_3NO_3, Na_2SO_4, and $NaNO_3$, respectively—in the wavelength range from 4 to 20 μm[39]. Table S1 of Supplementary Note 1 lists the IR absorption bands of $(NH_4)_2SO_4$ and Na_2SO_4 in IRW1[40–42]. The $\nu_3(SO_4^{2-})$ modes of $(NH_4)_2SO_4$ and Na_2SO_4 are strong absorption bands in IRW1 and would block heat transfer of thermal radiation to space. The radiative forcing caused by sulfate from fossil fuel and biofuel emissions has been estimated to be $-0.4\,\mathrm{W\,m^{-2}}$ (range: -0.6 to $-0.2\,\mathrm{W\,m^{-2}}$); for nitrate, it is estimated to be $-0.11\,\mathrm{W\,m^{-2}}$ (range: -0.3 to $-0.03\,\mathrm{W\,m^{-2}}$); the value for ammonium is included within the sulfate and nitrate estimates[12]. The effect of PM on global climate is uncertain because the effect of PM can be to cool or to warm, depending on its optical properties. In this study, we chose $(NH_4)_2SO_4$ for analysis because it is one of the major species of SIA, and because it features a strong absorption band and induces scattering in IRW1.

Comparison of absorption efficiency (Q_a) for different sizes of sulfate particles. Figure 2a, b presents the absorption cross-section (C_a) and absorption efficiency (Q_a) [where Q_a is the normalized C_a to the cross-section area of the particles] contours of $(NH_4)_2SO_4$ spheres, calculated by Mie theory, for wavelengths in the range from 4 to 20 μm, and for particle diameters (D_p) ranging from 0.1 to 10 μm (see Supplementary Note 2 for definitions of Q_a and C_a). The value of C_a becomes larger as the particle size increased, and is more obvious than 5 μm. In the normalized Q_a contour, all of the particle sizes resulted in three bands, corresponding to the three IR active vibration modes, at wavelengths of ~7, 9, and 16 μm. Two strong absorption bands
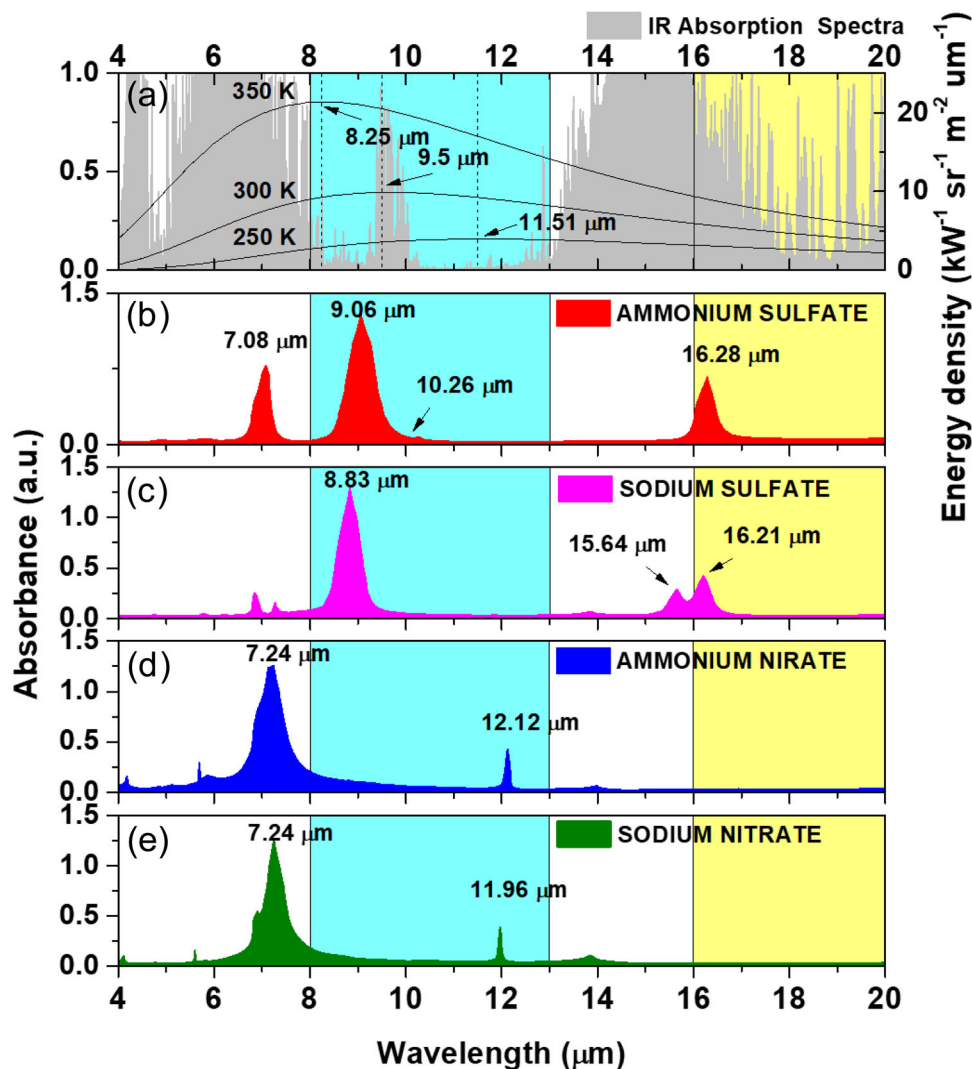
Fig. 1 Atmospheric IR absorption spectra and infrared absorption spectra of sulfate and nitrate. a Black-body emission curves of the Earth at various temperatures (black curves), with atmospheric IR absorption spectra at an air mass of 1.0 (gray area) as a reference. **b–e** IR absorption spectra of ammonium sulfate $(NH_4)_2SO_4$, sodium sulfate (Na_2SO_4), ammonium nitrate (NH_3NO_3), and sodium nitrate $(NaNO_3)$ in the wavelength range from 4 to 20 μm (Recalculated from Sigma Library of FT-IR Spectra).

for the particles having diameters of ~2 and 4 μm appeared at wavelengths of 9 and 16 μm, respectively, corresponding to the ED resonance of the $(NH_4)_2SO_4$ particles. The two strong absorption bands are included within IRW1 and IRW2, suggesting that these particles would greatly decrease the transparency of these IR windows—and intensify the greenhouse effect.

Figure 2c, d present the Q_a of $(NH_4)_2SO_4$ particles having values of D_p of 0.5, 2, and 2.5 μm ($PM_{2.5}$) and 5, 8, and 10 μm ($PM_{10-2.5}$), respectively. In Fig. 2c, the particle having a value of D_p of 2 μm gave the largest value of Q_a because of ED resonance at a wavelength of ~9 μm. In Fig. 2d, the values of Q_a of the particles having diameters of 5, 8, and 10 μm were not significantly different, but the absorption band became broader as the size increased. When the size of a particle increases, higher-order modes of resonance would dominate the Q_a spectrum. Further information about the values of Q_a for particles having different sizes is provided in the Supporting Information (see Supplementary Note 3 and Fig. S1 for detailed contribution of 2^n-poles analysis).

To verify the influence of the PM with different particle sizes in the IRW, we calculated (Fig. 2e) the maximum value of Q_a in IRW1, the average value of Q_a in IRW1, the maximum value of

Q_a in IRW2, and the average value of Q_a in IRW2. In the range of IRW1, the maximum value of Q_a for particle size D_p of 2 μm is 2.46. This Q_a peak arose from the ED resonance of the 2-μm particle. The average value of Q_a in IRW1 and IRW2 can represent a particle's influence on thermal radiation for the overall IRW1 and IRW2 absorption, respectively. Because resonance of high-order modes broadens the Q_a peak, the average values of Q_a in both IRW1 and IRW2 gradually increased upon increasing the value of D_p.

In general, atmospheric particles are normally classified into different modes according to their size, formation processes, and atmospheric age. Particles with a size between 0.01 and 0.1 μm (Aitken mode) account for the majority of the number of atmospheric particles, but they rarely account for more than a few percent of the total mass[13,16]. Particles with diameters between 0.1 and 1.0 μm (accumulation mode) usually account for a large portion of the total aerosol mass and have the largest surface area. This makes these particles performing significant importance to atmospheric chemistry. Particles <1.0 μm contribute to the optical properties of atmospheric aerosols. Although the particles with larger values of D_p provided higher average value of Q_a, the number of particles would decrease upon increasing the value of D_p. Both the
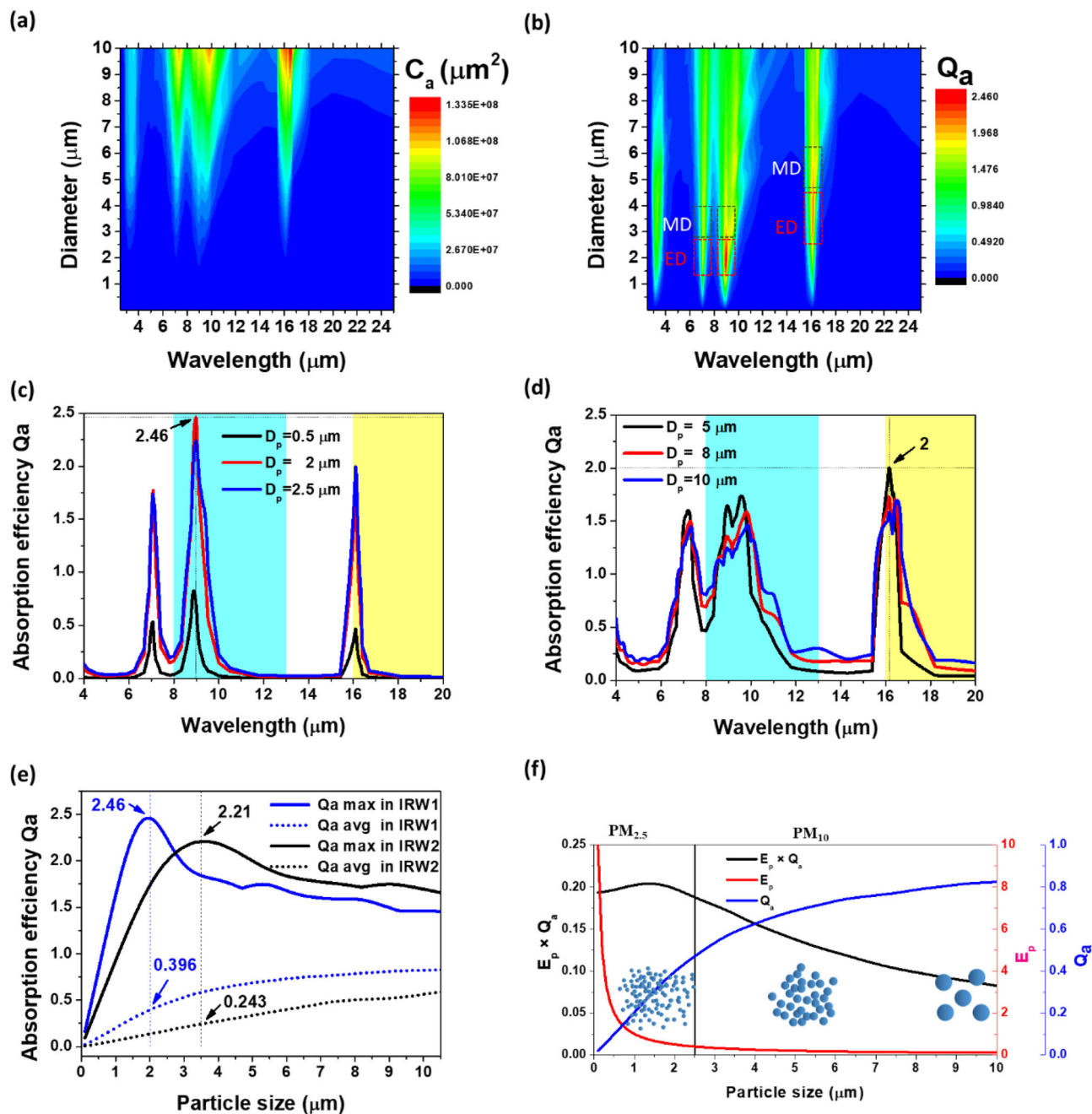
Fig. 2 Absorption efficiency coefficient Q_a for different sizes of sulfate particles. a, **b** Contour diagrams of the absorption efficiency factor (C_a) and (Q_a) of $(NH_4)_2SO_4$ particles for wavelengths in the range from 4 to 20 μm and for diameters (D_p) from 0.1 to 10 μm; **c** Q_a spectra obtained for values of D_p of 0.5, 2, and 2.5 μm; **d** Q_a spectra obtained for values of D_p of 5, 8, and 10 μm; **e** maximum and average values of Q_a obtained for values of D_p from 0.1 to 10 μm in IRW1 (blue and blue dotted curves) and IRW2 (black and black dotted curves); **f** trends in the average values of Q_a, the particle number effect (E_p), and the values of $Q_a \times E_p$ in IRW1 for various values of D_p.

number of particles and the value of Q_a should be considered when calculating the absorptance of these particles. We consider the number of particles and the value of C_a to calculate the absorptance of these particles with different sizes. At the same mass concentration, the number of particles is proportional to $\frac{1}{D_p{}^3}$, and the surface area is proportional to $D_p{}^2$. We define $\frac{1}{D_p}$ as the particle number effect (E_p), the values of $Q_a \times E_p$ can indicate the absorption capacity of particles with different sizes under the same mass concentration. Figure 2f displays the tendencies of the average value of Q_a, the value of E_p, and the value of $Q_a \times E_p$ in IRW1 for various values of D_p. Although particles of larger size provided higher average values of

Q_a, they would also introduce a decrease in the value of E_p. The value of $Q_a \times E_p$ reached a maximum at a value of D_p of 1.4 μm; it decreased when the value of D_p increased in the range of $PM_{10-2.5}$. As revealed in the curve of $Q_a \times E_p$, the overlapping part of the size distribution (1–3 μm) of fine particles and coarse particles would perform the greatest influence on thermal radiation absorption, and the influence of $PM_{2.5}$ on the absorption of thermal radiation would be greater than that of $PM_{10-2.5}$.

3D-FDTD simulations of the optical properties of SiO_2/sulfate core/shell mixtures. In the same way, we also analyzed the most
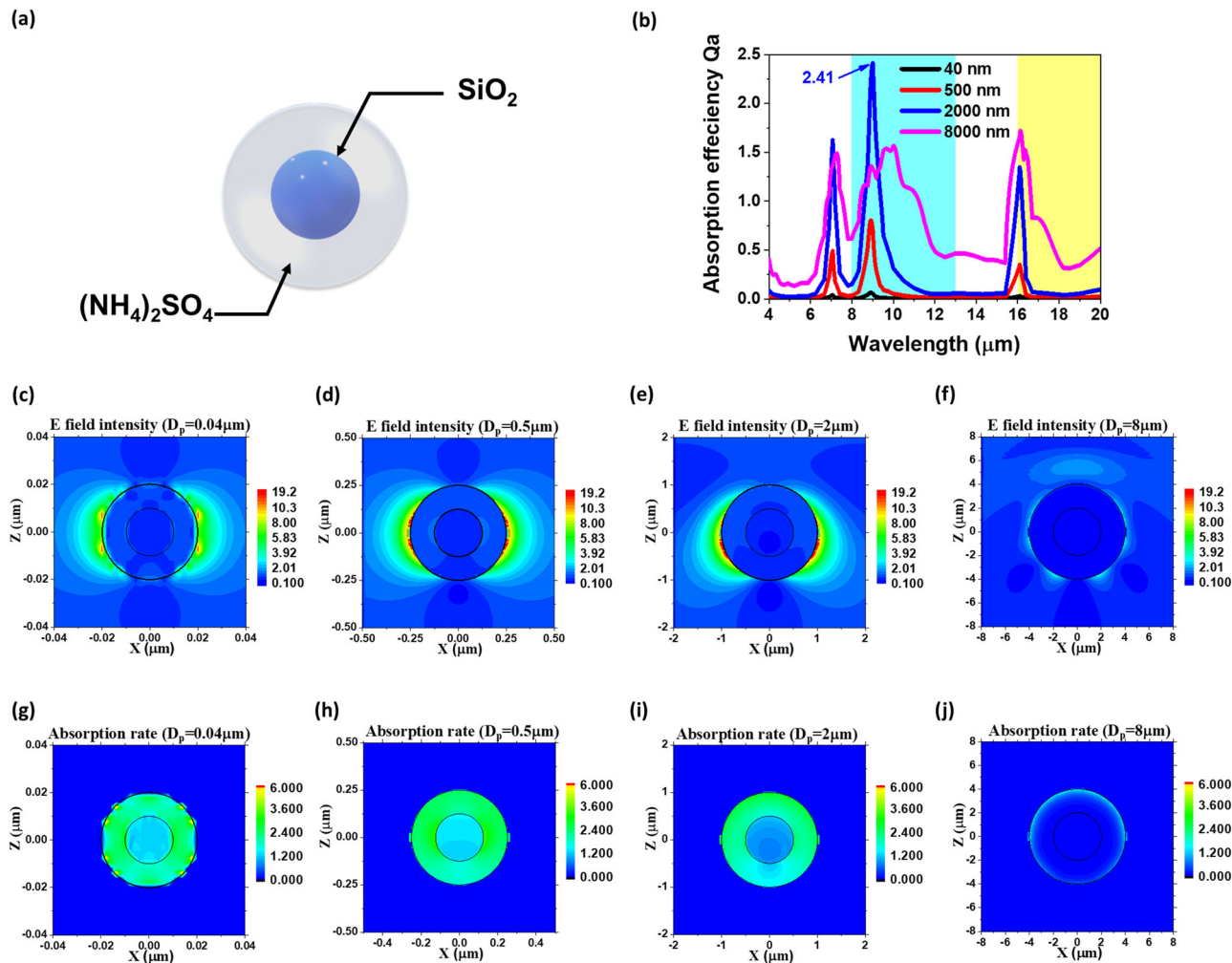
Fig. 3 The Q_a spectra and simulated E-field intensities and absorption rates of 0.04, 0.5, 2, and 8 μm core/shell structure particles. a Schematic representation of the core/shell structure, with SiO$_2$ as the core surrounded by a concentric spherical shell of (NH$_4$)$_2$SO$_4$. Here, the core/shell ratio is set at 0.5. **b** Q_a spectra of core/shell structures having values of D_p of 0.04, 0.5, 2, and 8 μm. **c–f** Simulated E-field intensities and **g–j** simulated absorption rates of **c**, **g** 0.04-, **d**, **h** 0.5-, **e**, **i** 2-, and **f**, **j** 8-μm core/shell structure particles.

abundant compound in the Earth's crust, silicon dioxide (SiO$_2$). The maximum value of Q_a appears around D_p of 2.5 μm at the wavelength of ca. 9 μm. The coating of atmospheric particles is often resulting from enhanced hygroscopicity due to aging mechanisms such as condensation, condensation, and heterogeneous chemical reactions[28,43]. To further investigate the optical behavior of PM, we used the 3D-FDTD method to simulate the electromagnetic field inside and around particles of various values of D_p. Aged PM may be fractionally or entirely encapsulated within a nearly spherical shell. We studied the optical properties of homogeneous sulfate and SiO$_2$/sulfate core/shell mixtures of PM (see Supplementary Note 4 and Fig. S2 for detailed homogeneous sulfate PM analysis). According to transmission electron microscope images[43], we assumed that silica or SiO$_2$ formed the core, coated by a concentric spherical shell of (NH$_4$)$_2$SO$_4$, Fig. 3a provides a schematic representation. The radius of the particle was 0.02, 0.25, 1, or 4 μm; the core/shell ratio was set at 0.5 and the core radius was 0.01, 0.125, 0.5, or 2 μm. Figure 3b presents the values of Q_a of core/shell particles having values of D_p of 0.04, 0.5, 2, and 8 μm for wavelengths ranging from 4 to 20 μm; the Q_a spectrum was similar to that of homogeneous (NH$_4$)$_2$SO$_4$, the optical properties of core/shell particles are dominated by the shell. For a value of D_p of 2 μm, the maximum value of Q_a of 2.54 occurred at a wavelength of 8.97 μm. Figure 3c–j present 3D-

FDTD simulations results of the normalized electric field intensities ($|E/E_0|^2$) and normalized absorption rates per unit volume ($P_{abs} = 0.5\omega\varepsilon_{image}|E/E_0|^2$ with the unit of W/m^3 (V/m)$^{-2}$) of the core/shell particle having sizes of 0.04, 0.5, 2, and 8 μm. All of the simulation results are normalized by the electric field intensity [with the unit (V/m)^2] of the incident light source. For the electric field distribution of the particle having a value of D_p of 0.04 and 0.5 μm (Fig. 3c, d), the shell thickness (0.01 μm and 0.125 μm) was smaller than the penetration depth of (NH$_4$)$_2$SO$_4$ ($d_p = \frac{\lambda}{4\pi k} = 0.43$μm), such that the light field could penetrate partially into the SiO$_2$ core. The extinction coefficient of SiO$_2$ at a wavelength of 9 μm ($k = 0.759$) is, however, smaller than that of (NH$_4$)$_2$SO$_4$ ($k = 1.665$). The penetrated light field and the lower extinction coefficient of SiO$_2$ result in a small absorption rate inside the SiO$_2$ core (Fig. 3g, h). The electric field distribution in (Fig. 3c, d) clearly reveal that although the electric field distributed on the outer edge of the particle shell, the area of spatial distribution of the high electric field regime for the particle of 0.5 μm is much larger than that of 0.04 μm. In Fig. 3e, i, the electric field distribution of the particle having a value of D_p of 2 μm reveals a dipole resonant pattern similar to that in the homogeneous case in Fig. S2. Because of the high absorption rate and small penetration depth of (NH$_4$)$_2$SO$_4$ particle having a value

of D_p of 2 μm, the light field had difficulty reaching the SiO₂ core. Most of the light was absorbed by the outer layer of $(NH_4)_2SO_4$; therefore, the values of Q_a were similar for both the core/shell ($Q_a = 2.54$) and homogeneous ($Q_a = 2.46$) cases at a wavelength of 9 μm and a value of D_p of 2 μm. Figure 3f, j present the electric field distribution and absorption rate pattern for the particle having a value of D_p of 8 μm. Here, the behavior in the core/shell case was very similar to that in the case of the homogeneous particle having a diameter of 8 μm. Because the shell thickness was much larger than the penetration depth of $(NH_4)_2SO_4$, the light could propagate in and be absorbed by only the $(NH_4)_2SO_4$ shell; it could not reach the SiO₂ core.

Scattering characteristics of sulfate particles. Furthermore, in this paper, we also calculated the scattering effect of the sulfate particles having diameters from 0.1 to 10 μm for wavelengths in the range from 4 μm to 20 μm. The results show that the scattering effect is much smaller than the absorption effect at longwave regimes (see Supplementary Note 5 and 6 for detailed scattering characteristics analysis). We also calculated the forward scattering efficiency (FWQ_s) and the backward scattering efficiency (BWQ_s). As the particle size increased, the value of $BWQ_s/(BWQ_s + FWQ_s)$ decreased. We suggest that backward scattering efficiency (BWQ_s) of particle diameter <5 μm is more important, because the smaller D_p, the more the number of particles and it would drive the scattering of thermal radiation back from the particles and, thereby, decrease the thermal emission going out to space beyond the atmosphere.

The changes in thermal power density of longwave radiation for different cases. To further explore the effect of PM on the thermal radiation balance of the atmosphere, we tested six cases (see Supplementary Note 7 for detailed case description). We estimated the absorptance of PM in the atmosphere by using the radiative transfer model. To estimate the warming effect P_{atm} of PM, we calculated the thermal radiation from the atmosphere in the absence and presence of PM. (see Supplementary Note 8 and 9 for detailed analysis of PM absorptance and P_{atm}). Table 1 presents the changes in thermal power density of longwave radiation for six different cases. The atmosphere displays positive radiative forcing, due to thermal radiation absorption by PM. Table 1 display three cases for homogeneous sulfate (case 1–3) and the other three cases for sulfate/SiO₂ core/shell mixtures (case 4–6) at various mass concentrations, respectively. The World Health Organization air quality model confirmed that 92% of the world's population lives in places where air quality levels of PM exceed the Air Quality Guidelines. The Air Quality Guidelines included in cases 1, 2 and 4, 5 as references should be reasonably representative in our calculations. In cases of severe air pollution, the warming effects of PM comprising homogeneous sulfate or sulfate/SiO₂ core/shell mixtures are 27.01 and 32.46 W m⁻², respectively (case 3 and 6). The longwave PM radiative effect may cause $(NH_4)_2SO_4$ to behave like a "greenhouse PM" or "greenhouse particles."

Comparison of atmospheric transmittance under clear sky and presence of PM. Figure 4 shows the atmospheric transmittance in the absence (clear sky) and presence of PM, including homogeneous sulfate and sulfate/SiO₂ core/shell mixtures at different concentrations. It can be clearly observed from Fig. 4a, b when the concentration of PM increases to 20, 50, and 1,180 μg m⁻³, the atmospheric transmittance decreased, especially in IRW1 (light-cyan areas). Sulfate has a strong absorption band around the wavelength of 9 μm, and the decrease in transmittance can be clearly observed. As far as we known, the injection of sulfate particle into the stratosphere is the most discussed proposal for solar geoengineering. However, in addition to the risk of ozone loss and heating of the lower tropical stratosphere[44], it is also likely to absorb the earth's radiation and warm the earth's surface. The atmospheric transmission spectra in the presence of homogeneous sulfate and sulfate/SiO₂ core/shell mixtures at same concentrations 1180 μg m⁻³ are shown in Fig. 4c. For the IR radiation absorbed by both sulfate and sulfate/SiO₂ core/shell mixtures, the transmittance of the core/shell mixtures case is lower than that of the homogeneous case, as shown by the dashed box. Because the light field could penetrate partially into the SiO₂ core of the set core/shell mixtures, the absorption rate of SiO₂ in the dashed box of spectral regime is greater than sulfate.

Conceptual experimental results. To confirm the thermal radiation behavior of $(NH_4)_2SO_4$ experimentally, we set up an apparatus to conduct a conceptual experiment in the laboratory. We prepared several samples containing 0.1 wt% $(NH_4)_2SO_4$ in KBr, and measured the cooling rate of different samples shielding (see Supplementary Note 10 and 11 for detailed experimental concept analysis). We found that the larger the shielding area, the slower the cooling rate. From this experiment, we suggest that the thermal radiation absorption of PM in the atmosphere would increase the temperature of the surroundings. The thermal emissivity of the samples composed of different $(NH_4)_2SO_4$ particle sizes was also measured. Different optical properties related to particle size have a significant effect on the thermal emissivity.

Conclusions

According to our findings in this study, sulfate displays strong IR absorption, especially in the atmospheric window. The IR absorption properties of $(NH_4)_2SO_4$ make it behave like "greenhouse PM" producing positive radiative forcing that may increase the temperature of its surroundings. An increase in the concentration of sulfate would reflect more of the incoming solar radiation back into space, but it would also capture more of the outgoing thermal radiation back to the Earth. $(NH_4)_2SO_4$ and sulfate/SiO₂ core/shell particles having diameter of ~2 μm display the maximum absorption efficiency factor (Q_a) of 2.46 and 2.54, respectively, at a wavelength of ca. 9 μm. At the same concentration, considering the factors of particle size and number together, the size of $(NH_4)_2SO_4$ particles with the strongest absorption capacity appears at 1.4 μm. The particle size also has an important influence on the scattering efficiency factor (Q_s), as the particle size decreases, the scattering phenomenon of

Table 1 The changes in the thermal radiation power density by different cases.

	Case 1	Case 2	Case 3	Case 4	Case 5	Case 6
Type	Homogeneous	Homogeneous	Homogeneous	Core/shell	Core/shell	Core/shell
Concentration (μg/m³)	20	50	1180	20	50	1180
P_{atm}	324.61	326.24	350.43	324.68	326.43	355.87
ΔP_{atm} (W m⁻²)	1.19	2.83	27.01	1.26	3.02	32.46

Presents the changes in the thermal radiation power density in atmosphere containing PM of various sizes and concentrations, including homogeneous sulfate and sulfate/SiO₂ core/shell mixtures.
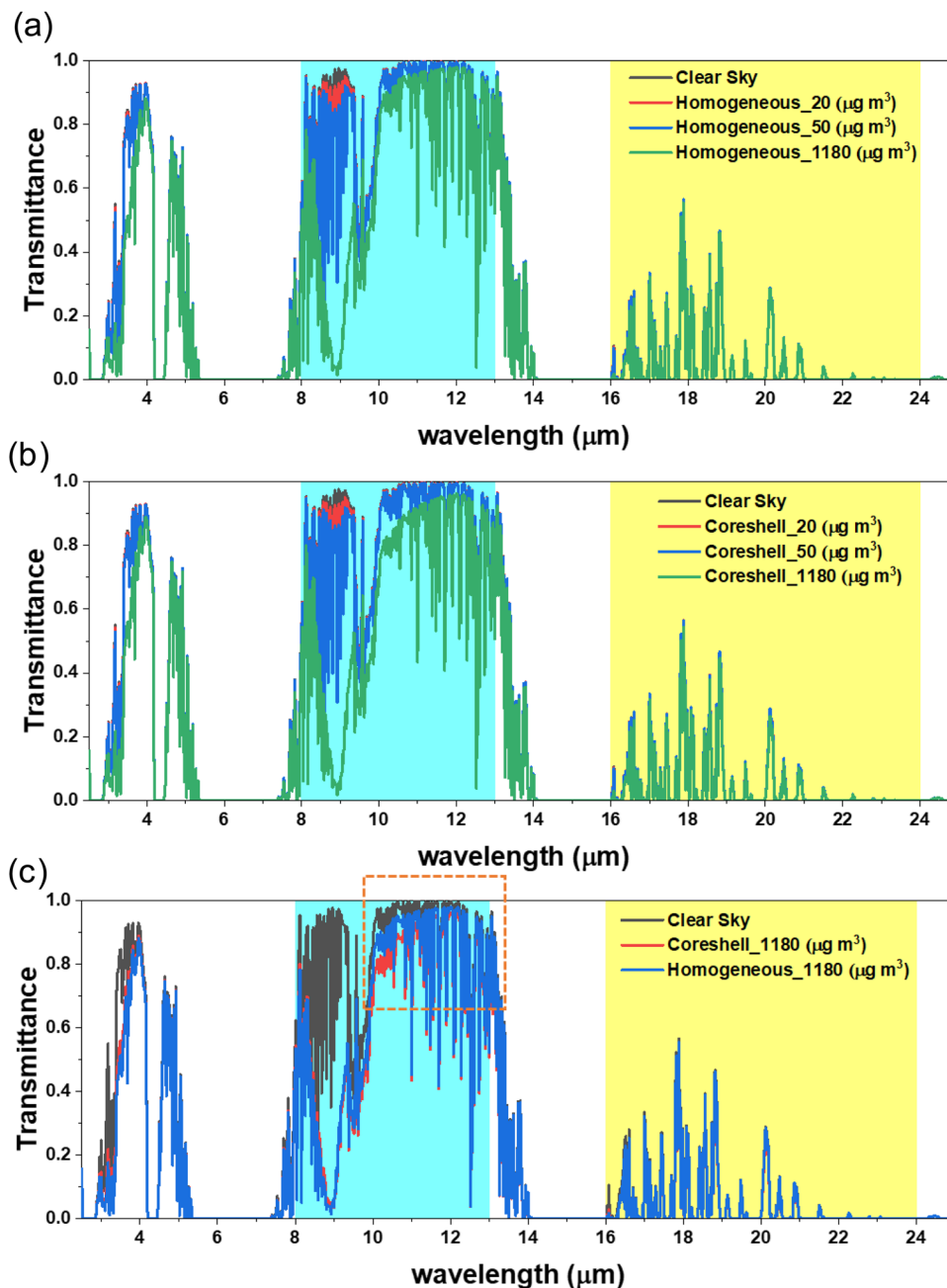
Fig. 4 The atmospheric transmittance in the absence and presence of PM. a Presence of homogeneous sulfate, and **b** Presence of sulfate/SiO$_2$ core/shell mixtures at different concentrations from 20, 50 to 1,180 µg m^{-3}. **c** Presence of homogeneous sulfate and sulfate/SiO$_2$ core/shell mixtures at same concentrations 1,180 µg m^{-3}.

(NH$_4$)$_2$SO$_4$ gradually becomes dominated by BWQ$_s$. The BWQ$_s$ would drive the thermal radiation scattered back from the particles of the PM, thereby decreasing the thermal emission going out to the space beyond the atmosphere. The absorption of particles at resonant conditions would be increased, even if the sizes of particles are much smaller than the wavelength. The relationship of particles size, absorption coefficients, and wavelength effect is very important for the investigation of resonance phenomena on particles. The simplified k distribution would lose the dependence of calculation results on wavelength. In this study, we used the LBL method to observe the resonance effect of PM particles with different sizes in broadband of spectral regime from 4 to 20 µm.

It is extremely difficult to describe the mixing state of an PM particle. In this study, we use simplified assumptions such as homogeneous (NH$_4$)$_2$SO$_4$ and sulfate/SiO$_2$ core/shell particles to discuss the effect of sulfate on thermal radiation absorption in IRW1 under resonance conditions Once the optical properties of various materials are known individually, the optical properties of mixed PM can be calculated and correctly averaged[45]. To evaluate how the longwave aerosol radiative effect varies as a function of size distribution and aerosol burden, we also briefly analyze the dependence of the longwave radiative effect as a function of median radius, distribution width, and sulfate/SiO$_2$ weight fraction to discuss the use of statistics data and treatment of uncertainties (see Supplementary Note 12 for a detailed discussion of

uncertainties). In this study, we only concern on the effect of IR resonance properties of SIA particles on LWPMRE without comparing it with a climate model. Comparison with climate models is difficult, but important to assess the quantitative impact of climate model on SIA. However, this is beyond the scope of this study, and we will analyze more PM species in future work and also investigate the LWPMRE of the aging process of the PM particles.

Methods

Sample fabrication. $(NH_4)_2SO_4$ and KBr were purchased from Sigma–Aldrich. The $(NH_4)_2SO_4$ and KBr particles were crushed to sizes of several hundreds of micrometers, using a bead crushing machine (Beads Crusher μT-12), and then ground in an agate mortar to sizes of a few micrometers. The $(NH_4)_2SO_4$ particles (particle sizes: ca. 2–20 μm) were mixed into KBr at a content of 0.1 wt%; the mixed powder was pressed into several tablets, using a tablet press. The $(NH_4)_2SO_4$ particles were observed through scanning electron microscopy (SEM, NOVA NANO 450). Fourier transform infrared spectroscopy (FTIR) was performed using a Fourier transform infrared spectrometer (Bruker VERTEX 70). The emissivity spectra of the samples in the mid- and far-infrared wavelengths (2.5–25.0 μm) were measured using the emissivity measurement kit (Emission Adapter, A540) and MCT detector of FTIR (Vertex 70, Bruker), and the blackbody furnace (IR-563/301. Blackbody system) was used as a correction source for the emissivity spectra. Temperature measurement data were recorded using K-type thermal couples and a paperless high-speed recorder (KR2000 Series Graphic Recorder).

Simulation method. High-resolution FTIR transmittance spectral data of $(NH_4)_2SO_4$, Na_2SO_4, NH_3NO_3, and $NaNO_3$ were obtained from the *Sigma Library of FT-IR Spectra*. The optical constant of $(NH_4)_2SO_4$ used in the simulations at a wavelength (λ) of 9 μm was $0.99 + 1.7i$. Mie theory was used to simulate the thermal radiation properties of the $(NH_4)_2SO_4$ particles. The absorption cross-section (σ_a) and the scattering cross-section (σ_s) were computed numerically using the Matlab code. The electric field distribution of the $(NH_4)_2SO_4$ particles was simulated using the 3D-FDTD method (RSoft FullWAVE).

Data availability

We did not use dataset. The raw data can be obtained from the following link (https://github.com/Gibss4987/data_of_PM) without restrictions. There are no restrictions on data availability. These data can be supplied as Supplementary Information, for reader convenience. Please contact us if you have any questions.

Code availability

The FDTD data is collected from commercial software (RSoft Fullwave). The data of Mie solution is performed and collected by home-made MATLAB code. The analysis of particle size is performed by ImageJ. The Code can be obtained from the corresponding author upon request.

References

1. Zhang, R., Sun, C., Zhu, J., Zhang, R. & Li, W. Increased European heat waves in recent decades in response to shrinking Arctic sea ice and Eurasian snow cover. *NPJ Clim. Atmos. Sci.* **3**, 1–9 (2020).
2. Wang, L., Yuan, X., Xie, Z., Wu, P. & Li, Y. Increasing flash droughts over China during the recent global warming hiatus. *Sci. Rep.* **6**, 1–8 (2016).
3. Cohen, J., Pfeiffer, K. & Francis, J. A. Warm Arctic episodes linked with increased frequency of extreme winter weather in the United States. *Nat. Commun.* **9**, 1–12 (2018).
4. Little, C. M. et al. Joint projections of US East Coast sea level and storm surge. *Nat. Clim. Change* **5**, 1114–1120 (2015).
5. Mengel, M., Nauels, A., Rogelj, J. & Schleussner, C.-F. Committed sea-level rise under the Paris Agreement and the legacy of delayed mitigation action. *Nat. Commun.* **9**, 1–10 (2018).
6. Schleussner, C.-F. et al. Differential climate impacts for policy-relevant limits to global warming: the case of 1.5 C and 2 C. *Earth Syst. Dyn.* **7**, 327–351 (2016).
7. Rogelj, J. et al. Differences between carbon budget estimates unravelled. *Nat. Clim. Change* **6**, 245–252 (2016).
8. Rogelj, J. et al. Paris Agreement climate proposals need a boost to keep warming well below 2 C. *Nature* **534**, 631–639 (2016).
9. Huang, Y. et al. Quantification of global primary emissions of PM2. 5, PM10, and TSP from combustion and industrial process sources. *Environ. Sci. Technol.* **48**, 13834–13843 (2014).
10. Haywood, J. & Boucher, O. Estimates of the direct and indirect radiative forcing due to tropospheric aerosols: a review. *Rev. Geophys.* **38**, 513–543 (2000).
11. Charlson, R. J. et al. Climate forcing by anthropogenic aerosols. *Science* **255**, 423–430 (1992).
12. Change, I. C. The Physical Science Basis. Contribution of Working Group I to the Fifth Assessment Report of the Intergovernmental Panel on Climate Change (Cambridge Univ. Press, 2007).
13. He, J. et al. Decadal simulation and comprehensive evaluation of CESM/CAM 5.1 with advanced chemistry, aerosol microphysics, and aerosol-cloud interactions. *J. Adv. Model. Earth Syst.* **7**, 110–141 (2015).
14. Zhou, C. et al. The impact of secondary inorganic aerosol emissions change on surface air temperature in the Northern Hemisphere. *Theor. Appl. Climatol.* **141**, 857–868 (2020).
15. Huang, R.-J. et al. High secondary aerosol contribution to particulate pollution during haze events in China. *Nature* **514**, 218–222 (2014).
16. Seinfeld, J. H. & Pandis, S. N. *Atmospheric Chemistry And Physics: From Air Pollution To Climate Change* (John Wiley & Sons, 2016).
17. Wilson, W. E. & Suh, H. H. Fine particles and coarse particles: concentration relationships relevant to epidemiologic studies. *J. Air Waste Manag. Assoc.* **47**, 1238–1249 (1997).
18. Granados-Muñoz, M. J. et al. Impact of mineral dust on shortwave and longwave radiation: evaluation of different vertically resolved parameterizations in 1-D radiative transfer computations. *Atmos. Chem. Phys.* **19**, 523–542 (2019).
19. Vogelmann, A. M., Flatau, P. J., Szczodrak, M., Markowicz, K. M. & Minnett, P. J. Observations of large aerosol infrared forcing at the surface. *Geophys. Res. Lett.* **30**, 57–1 (2003).
20. Otto, S. et al. Atmospheric radiative effects of an in situ measured Saharan dust plume and the role of large particles. *Atmos. Chem. Phys.* **7**, 4887–4903 (2007).
21. Perrone, M. & Bergamo, A. Direct radiative forcing during Sahara dust intrusions at a site in the Central Mediterranean: anthropogenic particle contribution. *Atmos. Res.* **101**, 783–798 (2011).
22. Sicard, M. et al. Intense dust and extremely fresh biomass burning outbreak in Barcelona, Spain: characterization of their optical properties and estimation of their direct radiative forcing. *Environ. Res. Lett.* **7**, 034016 (2012).
23. Meloni, D. et al. Determining the infrared radiative effects of Saharan dust: a radiative transfer modelling study based on vertically resolved measurements at Lampedusa. *Atmos. Chem. Phys.* **18**, 4377–4401 (2018).
24. Kok, J. F. et al. Smaller desert dust cooling effect estimated from analysis of dust size and abundance. *Nat. Geosci.* **10**, 274–278 (2017).
25. Adebiyi, A. A. & Kok, J. F. Climate models miss most of the coarse dust in the atmosphere. *Sci. Adv.* **6**, eaaz9507 (2020).
26. Li, J., Anderson, J. R. & Buseck, P. R. TEM study of aerosol particles from clean and polluted marine boundary layers over the North Atlantic. *J. Geophys. Res. Atmos.* **108**, 1 (2003).
27. Trochkine, D. et al. Mineral aerosol particles collected in Dunhuang, China, and their comparison with chemically modified particles collected over Japan. *J. Geophys. Res. Atmos.* **108**, 4–5 (2003).
28. Levin, Z., Ganor, E. & Gladstein, V. The effects of desert particles coated with sulfate on rain formation in the eastern Mediterranean. *J. Appl. Meteorol. Climatol.* **35**, 1511–1523 (1996).
29. Organization, W. H. *Health Aspects Of Air Pollution With Particulate Matter, Ozone And Nitrogen Dioxide: Report On A Who Working Group, Bonn, Germany 13-15 January 2003* (Copenhagen: WHO Regional Office for Europe, 2003).
30. Shi, N. N. et al. Keeping cool: enhanced optical reflection and radiative heat dissipation in Saharan silver ants. *Science* **349**, 298–301 (2015).
31. Hossain, M. M., Jia, B. & Gu, M. A metamaterial emitter for highly efficient radiative cooling. *Adv. Opt. Mater.* **3**, 1047–1051 (2015).
32. Zhai, Y. et al. Scalable-manufactured randomized glass-polymer hybrid metamaterial for daytime radiative cooling. *Science* **355**, 1062–1066 (2017).
33. Peng, Y. et al. Nanoporous polyethylene microfibres for large-scale radiative cooling fabric. *Nat. Sustain.* **1**, 105–112 (2018).
34. Hossain, M. M. & Gu, M. Radiative cooling: principles, progress, and potentials. *Adv. Sci.* **3**, 1500360 (2016).
35. Sadineni, S. B., Madala, S. & Boehm, R. F. Passive building energy savings: a review of building envelope components. *Renew. Sustain. Energy Rev.* **15**, 3617–3631 (2011).
36. Pacheco, R., Ordóñez, J. & Martínez, G. Energy efficient design of building: a review. *Renew. Sustain. Energy Rev.* **16**, 3559–3573 (2012).
37. Yin, X., Yang, R., Tan, G. & Fan, S. Terrestrial radiative cooling: using the cold universe as a renewable and sustainable energy source. *Science* **370**, 786–791 (2020).

38. Putaud, J.-P. et al. A European aerosol phenomenology–3: physical and chemical characteristics of particulate matter from 60 rural, urban, and kerbside sites across Europe. *Atmos. Environ.* **44**, 1308–1320 (2010).
39. Keller, R. *Sigma Library of FT-IR Spectra* (Sigma Chemical Co., 1986).
40. Fortin, T. J., Shilling, J. E. & Tolbert, M. A. Infrared spectroscopic study of the low-temperature phase behavior of ammonium sulfate. *J. Geophys. Res. Atmos.* **107**, AAC 4-1–AAC 4-9 (2002).
41. Weis, D. D. & Ewing, G. E. Infrared spectroscopic signatures of $(NH_4)_2SO_4$ aerosols. *J. Geophys. Res. Atmos.* **101**, 18709–18720 (1996).
42. Periasamy, A., Muruganand, S. & Palaniswamy, M. Vibrational studies of Na_2SO_4, K_2SO_4, $NaHSO_4$ and $KHSO_4$ crystals. *Rasayan J. Chem* **2**, 981–989 (2009).
43. Unga, F. et al. Microscopic observations of core-shell particle structure and implications for atmospheric aerosol remote sensing. *J. Geophys. Res. Atmos.* **123**, 13,944–913,962 (2018).
44. Keith, D. W., Weisenstein, D. K., Dykema, J. A. & Keutsch, F. N. Stratospheric solar geoengineering without ozone loss. *Proc. Natl. Acad. Sci. USA.* **113**, 14910–14914 (2016).
45. Toon, O. B., Pollack, J. B. & Khare, B. N. The optical constants of several atmospheric aerosol species: Ammonium sulfate, aluminum oxide, and sodium chloride. *J. Geophys. Res.* **81**, 5733–5748 (1976).

Acknowledgements

Author contributions

S.-L.C. and H.-L.C. conceived the study and analyzed main results. S.-L.C. wrote the paper. S.-W.C. contributed data and analysis. Y.-J.C. assists in the measurement of thermal emissivity in supplementary note 11. All authors contributed to data analysis and scientific discussion.

Competing interests

The authors declare no competing interests.

Additional information

Supplementary information The online version contains supplementary material available at https://doi.org/10.1038/s43247-021-00278-5.

Correspondence and requests for materials should be addressed to Hsuen-Li Chen.

Peer review information *Communications Earth & Environment* thanks the anonymous reviewers for their contribution to the peer review of this work. Primary Handling Editor: Heike Langenberg.

Reprints and permission information is available at http://www.nature.com/reprints

Publisher's note Springer Nature remains neutral with regard to jurisdictional claims in published maps and institutional affiliations.